JOURNAL OF Materials CHEMISTRY
Feature Article

High resolution electron microscopy in materials research

Gustaaf Van Tendeloo
EMAT, University of Antwerp, Groenenborgerlaan 171, B-2020 Antwerpen, Belgium

The historical evolution and the future aspects of high resolution electron microscopy are covered briefly. As for the applications for materials science and inorganic chemistry, we are positive about the future of electron microscopy, particularly when combined with other techniques. The strong interaction between sample and electron beam provides chemical, structural and electronic information through the emission of X-rays, inelastically scattered electrons, light, *etc*. We try to illustrate the strong points of high resolution electron microscopy with a few examples in different fields of solid state chemistry, including high T_c superconducting materials, colossal magnetoresistant materials and ionic conductors. The tendency of modern technology towards reduced dimensionality increases the importance of electron microscopy as a quality control device.

Introduction

Electron microscopy started with Ruska and Knoll who built their first electron microscope in 1931. The magnification was only 17 times, but it showed that an enlarged image could be obtained using accelerated electrons as information carriers. By 1933 Ruska obtained a resolution of 50 nm, which was an order of magnitude better than the resolution of the optical microscope. Its practical use, however, was not evident, since the accelerated electrons burnt any living material, which actually was the main purpose for the development. After 1945 materials scientists in particular realised the possible impact of electron microscopy and the instrument was further developed and underwent 'plastic surgery'. By that time the resolution of the instrument had decreased to the nanometer range and in 1956 Menter published the first lattice image of copper phthalocyanine; revealed a direct resolution of 1.2 nm and showed the presence of crystal defects such as dislocations. From that moment on, the idea of visualising individual atoms no longer remained a dream. In the early seventies Hashimoto and co-workers as well as Ottensmeyer *et al.* demonstrated a resolution of 2 Å and the direct observation of heavy atoms such as gold or thorium.

Now, at the turn of the century, most commercial electron microscopes have a resolution of around 2 Å and specially designed or high voltage high resolution microscopes reach the 1 Å level. Atomic resolution or structure resolution can therefore be performed on most inorganic materials. The focus is therefore no longer on the ultimate resolution, but on the application of this resolution in materials science. 'Frontiers of Electron Microscopy in Materials Science' should now become 'Frontiers in Materials Science by Electron Microscopy'. Electron microscopy has the enormous advantage of combining real space information down to the atomic scale with reciprocal space information in the diffraction pattern. This diffraction information can be obtained from areas of only a few nanometers in size. This makes electron microscopy a local probe, which is particularly strong at revealing the defect structure or the local structure of nano-scale inclusions. With modern technology entering nano-scale or even atomic-scale dimensions, electron microscopy has acquired a new goal: to guide scientists in 'tailoring' new materials.

This contribution will briefly outline the basics of electron microscopy and of high resolution electron microscopy in particular. We will then try to illustrate the possibilities of the technique for different problems in solid state chemistry or materials science.

Transmission electron microscopy (TEM)?

The idea of this introduction is not to provide a course in electron microscopy; for those interested we refer to specialised books such as the *Handbook of Microscopy*[1] or *Electron Diffraction Techniques*.[2] Our aim is rather to provide the basics of the technique and illustrate its possibilities as well as its limitations for practical problems.

The working principle of the electron microscope is closely related to that of the optical microscope; it is represented schematically in Fig. 1. Assume a plane wave of coherently accelerated electrons is incident on the sample under investigation. Within the sample, such a plane wave is no longer an eigenfunction of the system and generates different Bloch waves. If the sample is very thin, the wavefunction $f(x,y)$ at the exit plane of the object is not dependent on the thickness of the sample; in practice $f(x,y)$ will be the projected (crystal) potential. This exit plane will act as a planar source of spherical waves (a Huygens source). Through an electromagnetic lens (the equivalent of the optical lens) the diffracted beams are

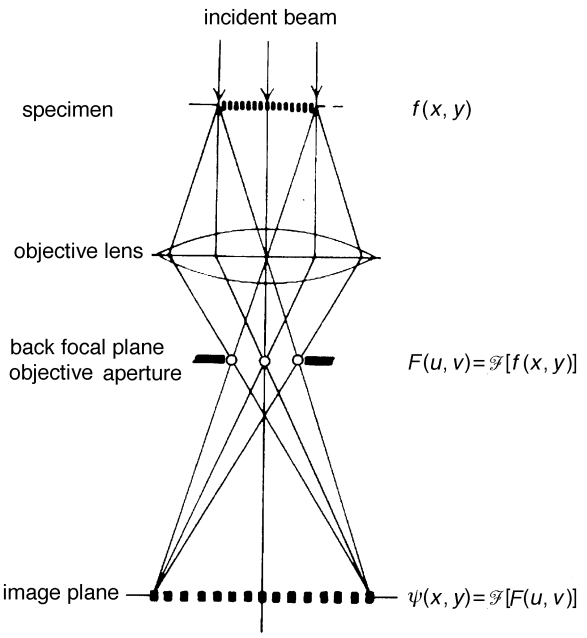

Fig. 1 Schematic representation of the image formation by the objective lens in an ideal transmission electron microscope

focused onto the back focal plane of this lens. The diffracted amplitudes of the different beams are given by the Fourier transform of the object function, *i.e.* $F(u,v)=\mathscr{F}[f(x,y)]$. If the object is periodic (*i.e.* perfectly crystalline), the diffraction pattern will consist of sharp spots; any deviation from perfection will result in scattering away from the sharp Bragg reflections. Because the interaction between the accelerated electrons and the material is very strong, electron diffraction is very sensitive to minor and local deviations from perfection. In a second stage of the imaging process, the back focal plane acts as a set of Huygens sources of spherical waves which again interfere in the image plane (Fig. 1). This is an inverse Fourier transform, which restores the object function:

$$\psi(x,y)=\{\mathscr{F}[F(u,v)]\}$$

The intensity in the image plane is then given by $|\psi(x,y)|^2$ and for this (ideal) microscope we obtain an enlarged image of the projected crystal potential.

The resolution limit for this ideal microscope which does not suffer from any lens aberrations, should be determined by only the sample and the wavelength of the accelerated electrons (Abbe's principle). In reality, microscope parameters such as spherical aberration, chromatic aberration or focus determine the resolution. Mathematically all these factors can be combined in the so-called 'transfer function', $\exp[i\chi(u,v)]$, which is nothing other than 'the way reality is distorted by the microscope'. The scattered amplitude in the image plane is then calculated as

$$\psi(x,y)=\mathscr{F}\{F(u,v)\exp[i\chi(u,v)]\}$$

In Fig. 2 we represent the imaginary part of this transfer function for a modern electron microscope at optimum defocus of the objective lens. Down to distances of $6\ nm^{-1}$ (*i.e. ca.* 1.7 Å in real space) the transfer function is largely negative and interpretation is relatively straightforward. For distances between 1.7 Å and 1.1 Å the structural details will be highly distorted by the fluctuating transfer function; below 1.1 Å no details are visible. This transfer function is very much a function of the focus of the objective lens and of the exact values of the spherical and chromatic aberration constants. Particularly for the correct interpretation of details below the Scherzer resolution limit (*ca.* 1.7 Å in this case) intensive computer simulations and retrieval methods are required. For more details on the retrieval of the projected potential using different methods, we refer to the contribution of Van Dyck in ref. 1.

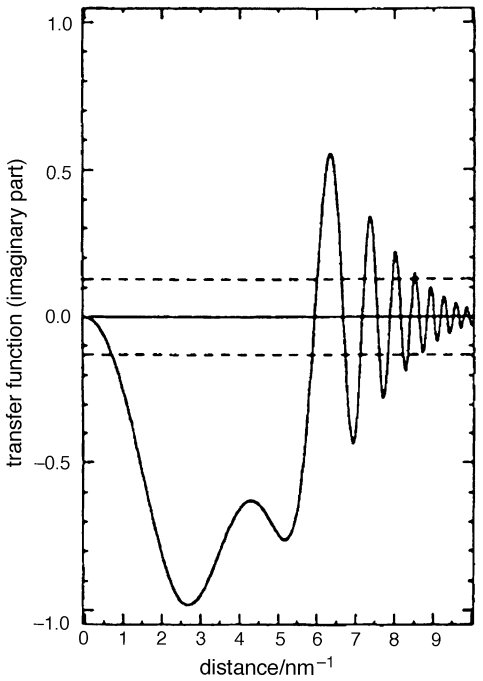

Fig. 2 Transfer function (imaginary part) of a high resolution electron microscope at optimum defocus; the horizontal dashed lines indicate the noise level

Finally, I would like to note that the term 'resolution of the microscope' is sometimes confusing: the resolution of the microscope can be expressed in terms of the Scherzer resolution limit (1.7 Å in Fig. 2) or in terms of the instrumental resolution limit (1.1 Å in Fig. 2).

Pros and cons of TEM

The fact that the interaction of accelerated electrons with matter is very strong has enormous advantages: only very small amounts of material are needed to perform the diffraction experiments and to obtain high quality images. The drawback of this strong interaction, however, is that the scattering is no longer kinematic and that the classical structure retrieval from diffraction evidence only (as in X-ray diffraction) is very difficult. Recently, however, with the installation of high quality CCD cameras on modern microscopes and with advanced retrieval methods, this problem can partly be solved. Details of this method and its application to solving the structure of nanometer sized precipitates can be found in the work of Zandbergen *et al.*[3]

Another problem, related to the strong electron–matter interaction present, is the easy absorption of accelerated electrons; one has to work in vacuum and the samples—or at least the interesting parts—have to be very thin; *i.e.* of the order of a few hundred nanometers for normal microscopy and below 20 nm for high resolution electron microscopy (HREM). Special sample preparation techniques therefore had to be developed, ensuring no damage to or alteration of the material under investigation. A widely used technique in materials chemistry is the so-called ion milling technique, where argon ions with an energy between 1 and 5 keV are bombarded on to a rotating sample at a glancing angle of between 1° and 15°. This technique is particularly useful when interfaces or grain boundaries are of interest. When only the bulk structure is of concern, the sample can just be crushed in an agate mortar and the powdered flakes then dispersed on a copper grid, covered with a lacy carbon film. This method holds for a large number of inorganic materials, as long as their anisotropy is not too large. Very anisotropic materials, such as graphite or dichalchogenides, can be prepared by cleavage between Scotch tape; the glue is dissolved in benzene or chloroform.

As mentioned before, I would like to underline that the interpretation of HREM images at the atomic level is not always straightforward. When the image is taken at the ideal Scherzer defocus, for very thin regions, with a short periodicity along the electron beam direction, with the electron beam perfectly along a low order zone axis, on a perfectly aligned microscope, the heavy atoms tend to be imaged as black dots and interpretation will not cause too many problems down to the Scherzer resolution limit. All other cases, however, will generally require simultaneous computer image calculations for different defocus and thickness values. The effect of a number of these deviations from perfection can be simulated by the computer. This is particularly important for a slight misalignment of the crystal or of the microscope; even if the average orientation of the crystal is perfect, local deviations tend to occur in the vicinity of crystal imperfections, incoherent precipitates, *etc.*

Most recent electron microscopes no longer have LaB_6 type filaments but field emission sources; these provide not only a more intense beam but also a more coherent beam, which results in a transfer function as in Fig. 2, where the information limit is pushed further beyond the Scherzer resolution limit.

Correct quantitative interpretations in this region as a function of the projected crystal potential can no longer be done on a single image; one needs a series of images at different defocus values in order to retrieve the projected crystal potential. This method has now proven its usefulness in unravelling crystal structures of nano-crystalline domains. In combination with the quantitative analysis of the electron diffraction patterns this has become a powerful technique in crystallography. More details on the technique can be found in refs. 3 and 4.

One should also realise that most published HREM images are taken at room temperature. Electron microscopy is possible between liquid He temperature and about 1000 °C but at temperatures different from ambient temperature the effects of heating or cooling seriously hamper the resolution. The resolution is then no longer governed by the aberrations of the lens, but by the stability of the specimen stage. Practically this means that at temperatures different from ambient temperature, a point resolution below 2.5–3.0 Å is extremely hard to obtain.

HREM combined with other microscopy techniques

HREM by itself may be highly informative and produce spectacular images; the strength of electron microscopy is mainly in its combination with several techniques within the same instrument, on the same specimen area. While HREM provides real space information, the electron diffraction pattern provides complementary information on the sample. The so called convergent beam electron diffraction (CBED), in particular, will provide information on the local lattice parameters and the local symmetry (point group as well as space group).

The total electron–sample interaction is a very complex phenomenon and elastic scattering—used for imaging—is only one of the effects (see Fig. 3). The incoming high energy electron is also at the origin of the production of X-rays, light, Auger electrons, back scattered electrons, inelastically scattered electrons, *etc*. All of these electrons, X-rays and photons carry information on the sample area irradiated by the incoming electrons. Since the electron beam can be focused down to 1 nm or even smaller, local chemical or electronic information is readily available. The most developed and practically applicable methods are EDX (energy dispersion of X-rays) and EELS (electron energy loss spectroscopy). EDX analyses the outcoming X-rays which provide quantitative information on the local composition, particularly the heavier elements. EELS also provides chemical information—particularly for the lighter elements—but is also sensitive to the binding of the considered element (*e.g.* it will easily differentiate the sp^2 binding in graphite from the sp^3 binding in diamond). These chemical

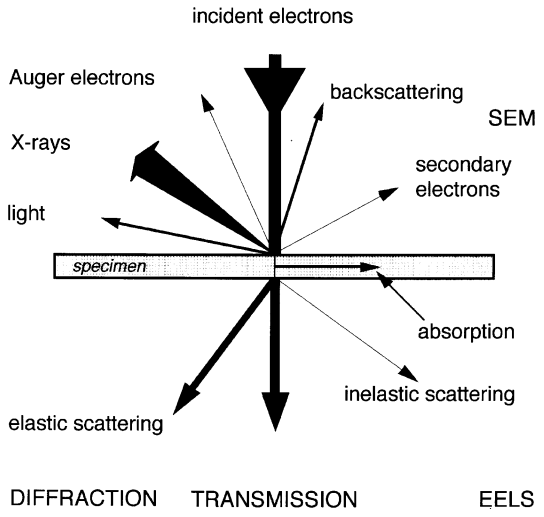

Fig. 3 Schematic representation of the electron–specimen interaction for high energy electrons (100 kV or more)

methods (*e.g.* in determining the exact oxygen content) are less quantitative than some of the classical chemical methods, but these determinations are local and are particularly useful for determination of deviations from an average composition or to detect local fluctuations in the composition. Exactly how quantitative the EDX and EELS methods are is hard to define explicitly; it depends on a number of parameters such as the specific elements present in the compound, the size of the domain investigated, the availability of a standard with a fixed composition, *etc*.

Structure of fluorinated $YBa_2Cu_3O_6F_x$ through HREM

The possibility of synthesising new superconducting materials is limited by the problem of maintaining electroneutrality and matching between different chemical bonds in their layered structures. This problem can be reduced significantly and, therefore, new superconductors can be prepared if oxygen anions located in the insulating blocks are replaced by fluorine. O^{2-} and F^- anions have different charges but possess similar atomic radii and may form similar structures. The preparation of Cu-based oxyfluorides, however, is often made difficult by the high stability of simple fluorides or oxyfluorides; the use of soft chemistry techniques can therefore be a powerful tool in overcoming this problem and preparing new materials. For the fluorination of the high T_c superconducting compound $YBa_2Cu_3O_7$ (YBCO), XeF_2 can be used successfully as a fluorinating reagent at temperatures not higher than 300 °C. The resulting compound $YBa_2Cu_3O_{6+x}F_y$ is also superconducting ($T_c = 94$ K).

With the aim of obtaining Cu-containing superconductors, a fluorination treatment should keep the CuO_2 layers unaltered. Many researchers tried to substitute oxygen by fluorine but they obtained either multiphase mixtures or partially fluorinated compounds with lower T_c values than that for pure $YBa_2Cu_3O_7$. In the case of YBCO an anion deficient starting material is definitely needed since anion exchange in oxidised YBCO demands higher temperatures leading to the formation of very stable admixtures. Using HREM we determined the crystal structure of the new material and using EDX we provided proof that fluorine has definitely entered the structure.

$YBa_2Cu_3O_{6.95}$ and $YBa_2Cu_3O_{6.11}$ formulations were used for fluorination. All subsequent operations, including the fluorination, were carried out in a glove box in a dried N_2 atmosphere. Syntheses were carried out in Ni crucibles placed in a hermetically sealed steel or Ni container. More details on the preparations can be found in ref. 5.

The fluorination of $YBa_2Cu_3O_{6.95}$ did not lead to any significant changes in the structure or to a change in T_c, which led us to conclude that in this case there is no noticeable insertion of fluorine into the structure or a replacement of O atoms by F atoms.

The fluorination of $YBa_2Cu_3O_{6.11}$, however, revealed a strong dependence of the properties and the (micro)structure on the synthesis conditions and annealing temperature. The highest value of $T_c = 94$ K was found after 50 h at 350 °C. The fluorinated samples exhibited a large volume fraction of superconducting phase, which confirms the bulk nature of the observed superconductivity. The fact that no orthorhombic YBCO phase was observed on ED or HREM images implies that the superconducting transition can only be attributed to the fluorinated phase. EDX measurements inside the electron microscope indicate that fluorine had indeed entered the crystal structure of YBCO. However, the fluorine concentration varied between different grains and even within a single grain.

The insertion of fluorine into the YBCO structure may occur at two different positions. The most probable is occupation of positions in the Cu(1) layer. When up to one fluorine atom per unit cell is incorporated, the fluorine may either occupy

one of the two available oxygen positions in the Cu(1) layer and form a square Cu(1) co-ordination polyhedron or it may be distributed statistically on the 1/2,0,0 and 0,1/2,0 sites. In the first case such intercalation should be accompanied by an orthorhombic distortion of the initial tetragonal unit cell similar to the case in the $YBa_2Cu_3O_7$ structure. A statistical arrangement would maintain tetragonal symmetry. We will call this the F1 phase [Fig. 4(*a*)]. If the fluorine content is more then one atom per unit cell (F2 phase), the extra atoms will occupy the remaining sites in the Cu(1) plane. The presence of two F atoms in this plane results in the formation of an octahedral co-ordination for the Cu(1) atoms [Fig. 4(*c*)]. Such an arrangement will lead to a distortion of the octahedra due to a Jahn–Teller effect and a substantial increase of the Cu(1)–Cu(2) separation. An increase of the Cu(1)–O distance (from *ca.* 1.90 Å in reduced YBCO to 2.3–2.5 Å in the F2 phase) will lead to a *c*-parameter for the new F2 phase of about 13.0 Å. Obviously, such fluorination will result in the oxidation of the Cu atoms and keep the superconducting CuO_2 layers unaltered.

A second possibility for the intercalation of fluorine in the YBCO structure is to insert it into the Y layer. This, however, will automatically suppress superconductivity because the F atoms will create a fluctuation of the charge density and induce hole localisation.

The combination of diffraction and high resolution microscopy (HREM) allowed us to determine the approximate structure while EDX unambiguously confirms the presence of F even on a nanometer scale. The [001]* diffraction pattern of Fig. 5(*a*) shows an intensity and spot distribution typical of tetragonal symmetry with $a = 3.86$ Å. The overwhelming majority of the crystals show this type of tetragonal symmetry, without the presence of extra reflections or diffuse streaks. While the [001]* patterns are the same for all crystals, two different patterns are observed along [*hk*0]*; this is illustrated in the [100] and [110] sections of Fig. 5(*b*)–(*e*). Such patterns can be obtained from neighbouring areas, even within the same crystal, as indicated in Fig. 6.

Patterns 5(*c*) and 5(*e*) exhibit clear and well defined reflections, which can all be indexed in a tetragonal cell with $a = 3.869$ Å and $c \approx 11.66$ Å; *i.e.* very closely related to the undoped YBCO. The sharp reflections as well as the absence of streaks reveal a perfectly crystalline structure; they are typical of the F1 phase.

The [100]* zone of Fig. 5(*b*) on the other hand exhibits

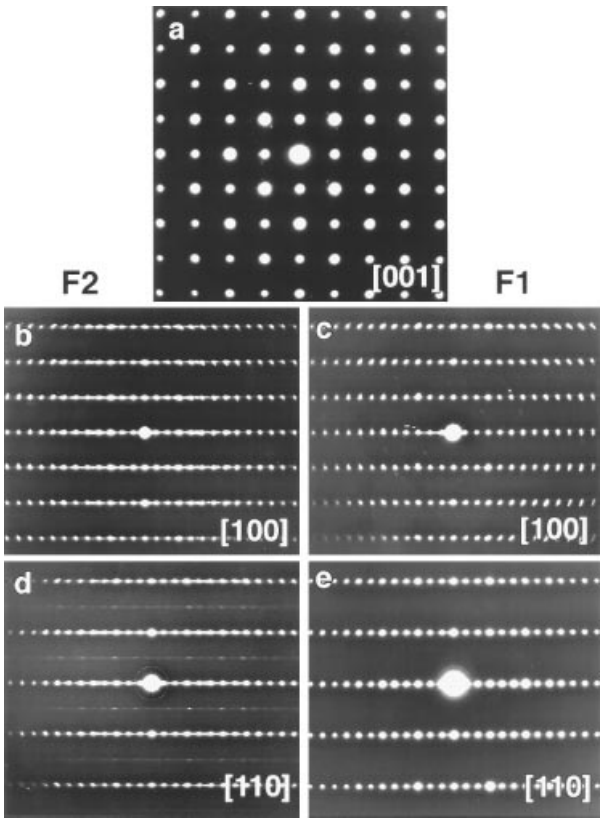

Fig. 5 Electron diffraction patterns of the main reciprocal zones for the F1 and F2 phases. The [001]* zone is common to both compounds.

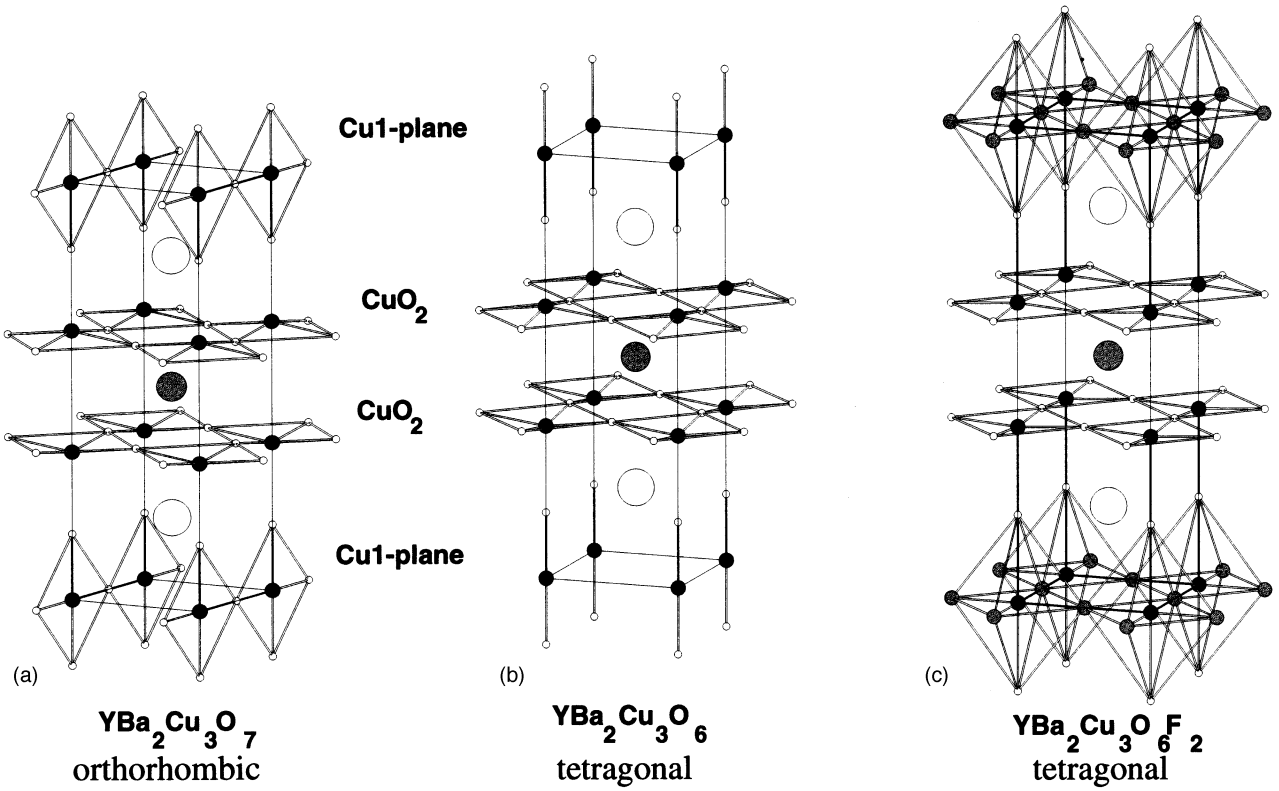

Fig. 4 Schematic crystal structures of: (*a*) orthorhombic $YBa_2Cu_3O_7$, (*b*) tetragonal $YBa_2Cu_3O_6$, (*c*) fully fluorinated $YBa_2Cu_3O_6F_2$

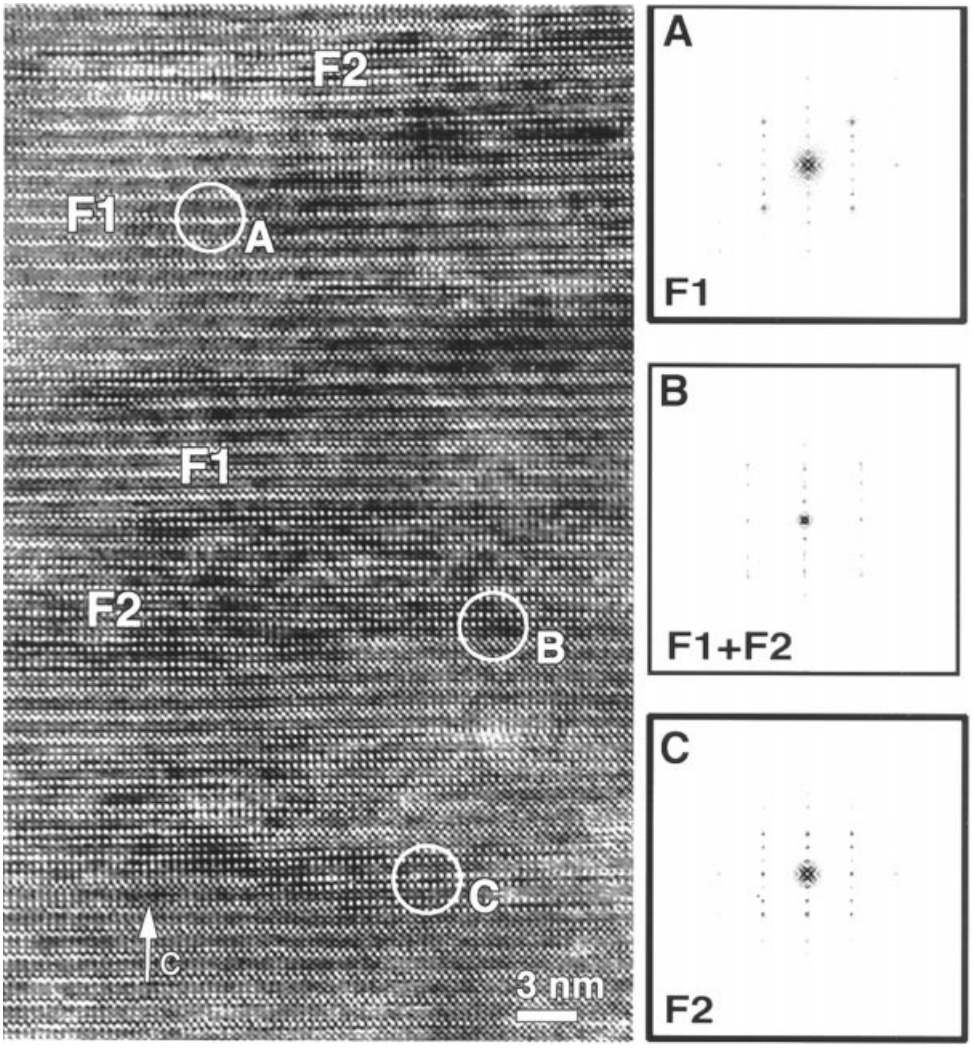

Fig. 6 HREM image of fluorinated YBCO material, together with the optical diffraction patterns obtained from different areas of the HREM image, corresponding to phases F1 (A), F2 (C) and the interface (B) between F1 and F2

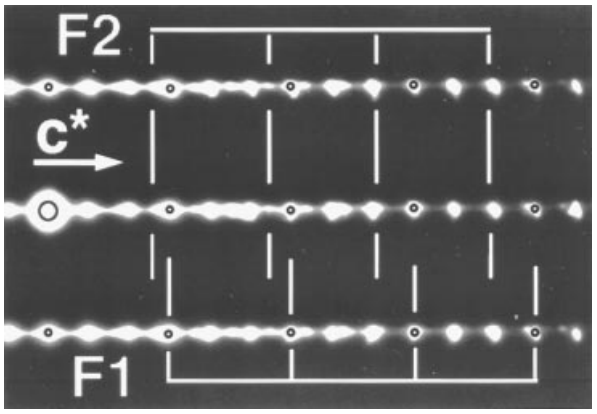

Fig. 7 Enlarged ED pattern along [100]* (from Fig. 5d) illustrating the presence of F1 and F2 phases with different c^* parameter. Only reflections with $l=3n$ are marked.

pronounced diffuse streaks along the c^* axis. Such streaking may arise due to the presence of a large amount of planar (001) defects in the F1 phase. A detailed examination of such ED patterns indicated the periodic presence along c^* of extra intensity maxima apart from the maxima due to the F1 phase (Fig. 7). These reflections are compatible with a new unit cell with lattice parameters $a=3.869$ Å and $c\approx13$ Å. This phase we will call the F2 phase. It is clear, however, that, in contrast to the F1 phase, the F2 phase does contain a large number of planar defects, inducing streaking of the reflections along c^*. Diffraction patterns along the [110]* zone axis [Fig. 5(*d*)] not only exhibit streaks along the c^*-axis but very often also show additional streaks (or rows of diffuse spots) parallel to the c^*-direction at positions $h+1/2$, $k+1/2$, l. This would imply that the structure determination of the F2 phase as tetragonal with $a=3.869$ Å and $c\approx13$ Å is only a first approximation. The real unit cell would be something like $a\sqrt{2}\times a\sqrt{2}\times c$. The exact origin of these extra reflections, however, is not clear at this stage.

[100] HREM images are able to elaborate the difference between the F1 and the F2 phase. The F1 phase shows a contrast very similar to that for the undoped YBCO (Fig. 8). Direct measurement of the c/a ratio, from the HREM image or by using the Fourier transform of limited parts of the HREM images (see, *e.g.*, Fig. 6A) allow us to deduce the c-parameter as 11.7 Å, which is in good agreement with the corresponding X-ray data.

The F2 phase, with an enlarged c-parameter, exists as an intergrowth within the F1 matrix (Fig. 6) or occurs as an isolated defect with a limited extension (see below). Optical diffraction obtained from areas corresponding to the phases F1 and F2 (marked A and C respectively in Fig. 6) and its interface (marked B) confirm the ED data. The difference in the c-parameter for the F1 and F2 phases is clearly visible in the enlarged Fig. 9. Using the F1 phase as an internal standard, we obtain a c-parameter of 13.0–13.2 Å for the F2 phase. It is clear visually that in the F2 phase, the distance between the

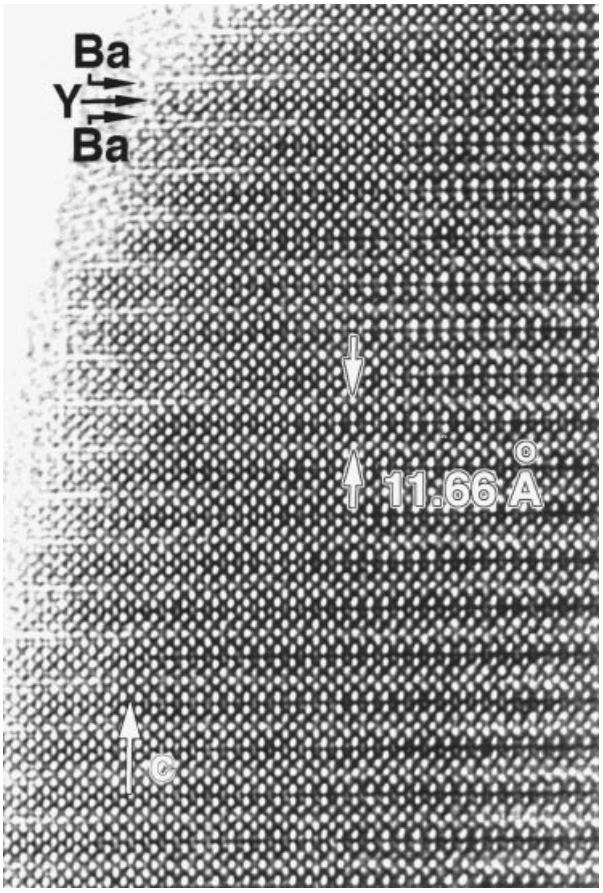

Fig. 8 HREM image along [100] for the F1 phase; no defects are detected over large areas but EDX measurements indicate the presence of fluorene

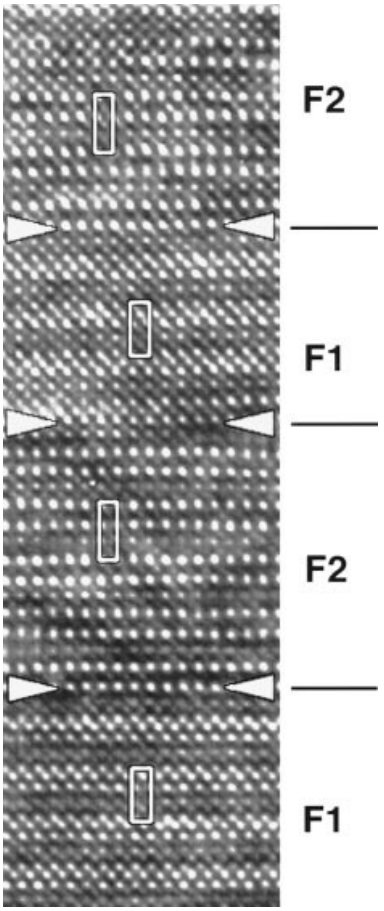

Fig. 9 Enlarged area showing an alternation of F1 and F2. The corresponding unit cells are indicated; the difference in the *c*-axis is obvious.

Cu(1)–O layer and the neighbouring BaO layers has increased drastically, pointing towards a fluorine uptake within the Cu(1) plane.

In order to determine the stacking sequence for this new structure we performed image simulations for different models based on partially and fully fluorinated structures. For the F2 phase we assumed that in the Cu(1) plane all the oxygens have been replaced by fluorine, leading to a structural formula $YBa_2Cu_3O_6F_2$. The atomic coordinates were deduced according to the larger unit cell, taking into account a change of the Cu(1)–O(apical) separation due to a Jahn–Teller effect. The Cu(2)–Cu(2) distance was kept unaltered with respect to the undoped YBCO. A structural model for the new $YBa_2Cu_3O_6F_2$ compound is shown in Fig. 4(*c*). Calculated images for different thicknesses and defocus values, based on the above models show a reasonable agreement with the experimental images. The remaining difference between the calculated and the experimental images is attributed mainly to the presence of local strains due to the intergrowth of the F1 and the F2 phases.

Electron diffraction, as well as direct images, indicates a high interweaving of the F1 and F2 phase. The F2 phase never exists over large areas but mainly occurs as bands within an F1 matrix (see Fig. 6). These bands are more or less parallel to the (001) planes but there is no rigid interface. In less fluorinated material, F2-type intercalation exists as isolated defects within an F1 matrix; an example is shown in Fig. 10. The extra wide separation between the Cu(1)–O layer and the surrounding BaO layers means that the atom planes are no longer straight but become wavy when a 'pancake' of fluorine is intercalated. In material which has been less fluorinated such defects are actually the only direct sign of fluorination. It is clear that such isolated defects act as the nucleus for the fluorination process and the formation of the F2 phase.

HREM of materials exhibiting colossal magnetoresistance

Recently colossal magnetoresistance (CMR) has been discovered in different manganese perovskite materials with general formula $(Ln_{1-x}A_x)MnO_3$ with Ln = La, Pr, Nd, Sm and A = Ba, Ca, Sr. For some of these materials the ratio between the resistance in zero magnetic field and the resistance in a 5 T magnetic field can be as high as 10^{11}. The exact origin of this effect is still under debate, but it is clear that two important parameters are driving the magnitude of the magnetoresistance: the number of itinerant holes and the length and direction of the Mn–O bond. The first is directly connected to the oxidation state of the Mn ion (the ratio of Mn^{4+} to Mn^{3+}); the second parameter is connected to the average size of the interpolated cation in the perovskite structure. These parameters have in a number of cases been optimised leading to the reported magnoresitance values.

The average room temperature structure has been determined by other diffraction techniques as orthorhombic with symmetry *Pnma* and with lattice parameters $a \approx a_p\sqrt{2}$; $b \approx 2a_p$; $c \approx a_p\sqrt{2}$. Electron microscopy shows the presence of a large number of orientation variants (domains related by a rotation of 90°); most electron diffraction patterns therefore show a superposition of the different orientation variants. HREM images can be obtained along most of the low index zone axes and clearly allow us to separate these different variants (Fig. 11). The contrast is not only thickness dependent (as expected), but also region dependent. Such changes are often observed in the microscope and generally are attributed to local changes in the crystal orientation or in the height of the sample (*i.e.* the focus of the sample). In the present case, however, it was verified that these effects did not play. Moreover, in most parts of the image the 0.77 nm spacing ($2a_p$

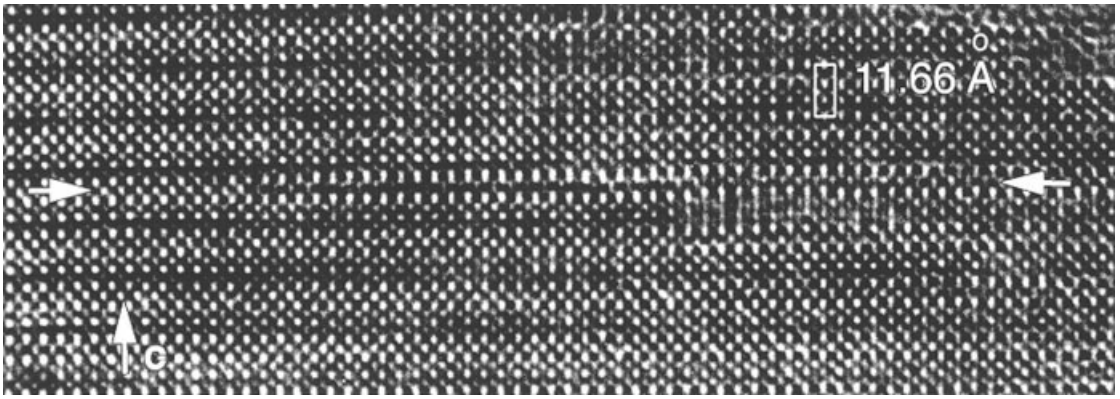

Fig. 10 The intercalation of fluorine into the Cu(1) layer occurring as an isolated defect (indicated by arrows); HREM image along [100]

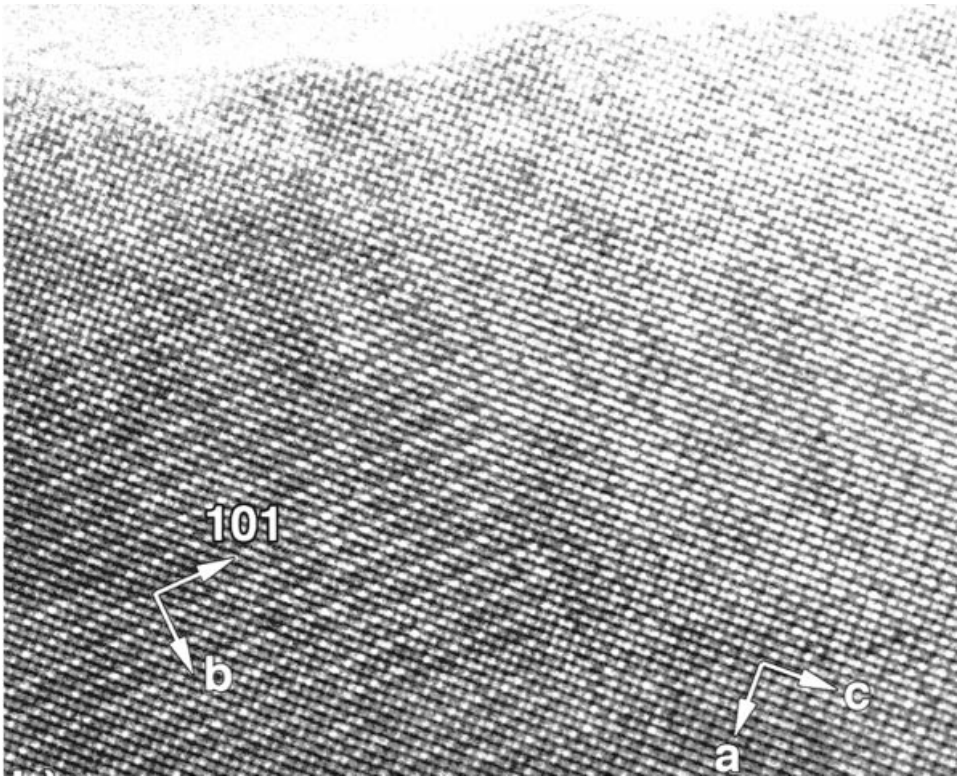

Fig. 11 HREM image of $Nd_{0.5}Ca_{0.2}Sr_{0.3}MnO_3$ across a twin boundary. Note the change in contrast and the pronounced $2a_p$ contrast along the *b*-axis in the left domain.

spacing along the *b*-axis) is clearly observed (see left lower part of Fig. 11). In the calculated images for different focii and different thicknesses, this doubling of the unit cell is never observed. Even including slight tilts, small misalignments or inclusion of the influence of upper Laue zones did not produce the correct experimental images. Careful inspection of the HREM images, and comparison with the calculated images, revealed that the double periodicity is related to the $(MnO)_2$ layer in particular. As soon as we introduce a monoclinic distortion, creating space group $P2_1/c$, by slight displacements of the oxygens in the $(MnO)_2$ layer, the calculated images fit the experimental ones. The calculated diffraction patterns remain in agreement with experiment. The atom shifts involved are less than 5%.

As in most superstructures, based on a high symmetry parent structure—the perovskite structure in this case—twin boundaries and antiphase boundaries occur regularly. Depending on the exact composition and the preparation method, the density of these two-dimensional defects can be varied. Independent of composition or preparation, however, another type of defect occurs in almost all of the perovskite-based CMR materials: they are isolated point-like defects, clearly visible in the [101] images [Fig. 12(*a*)]. In this image the bright dots can be correlated with the positions of the (Pr, Ca, Sr) sites in this case while the lower intensity dots are associated with the Mn configuration. The intensity of the (Pr, Ca, Sr) sites is very constant, as can be seen from the horizontal scan in Fig. 12(*b*). The intensity of the Mn dots, however, varies considerably within a limited area [see also the scan in Fig. 12(*c*)]. Care is taken to make sure that these defects are not introduced by the intense electron beam used for HREM observations; *i.e.* the density of defects does not alter with observation time. One could visualise three origins for these defects: (i) vacancies or atomic substitution on the Mn sites, (ii) oxygen vacancies in the MnO_6 octahedra, and (iii) variation of the oxygen environment around the manganese. Neutron, as well as EDX measurements, do not show any significant deviation of the oxygen or the Mn content; the high density of defects can therefore only be explained by a local modification of the manganese environment. Taking into account the Mn^{III} and Mn^{IV} mixed valence, the variation of contrast is probably closely related to a local ordering of Mn^{III} and Mn^{IV}, so that

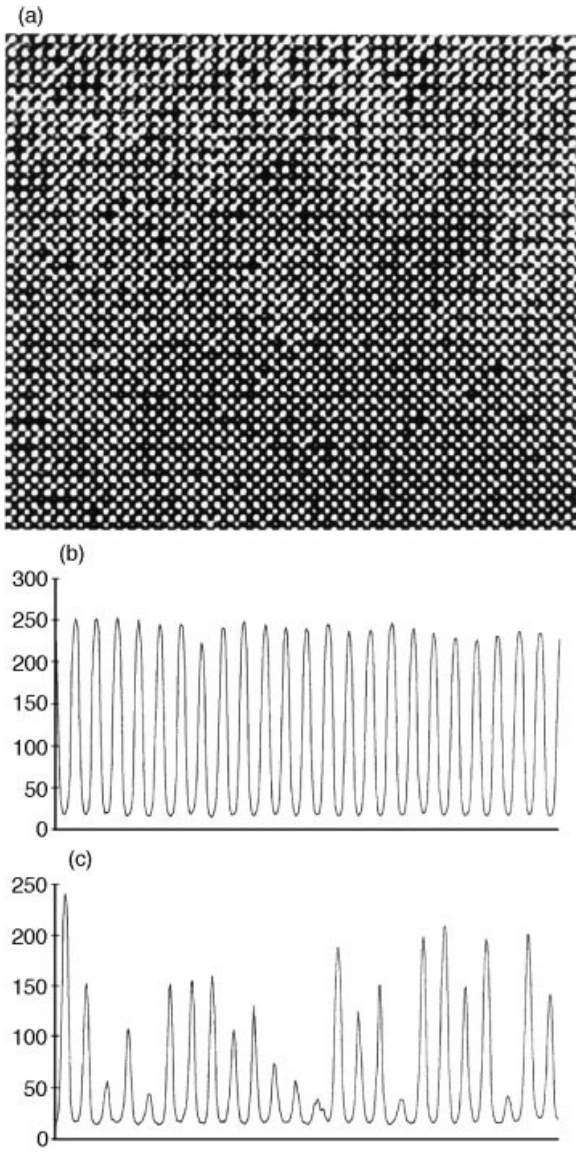

Fig. 12 (*a*) HREM image of $Pr_{0.75}Sr_{0.25}MnO_3$ along [101]. The heavy cations are imaged as intense bright dots, the manganese positions as smaller bright dots. Intensity variations at the Mn positions are particularly evident. (*b*) A (horizontal) scan along the Ln bright lines. (*c*) A scan along the Mn less intense lines.

a variation of the Mn–O distances around the manganese would be involved, in agreement with the different sizes of Mn^{III} and Mn^{IV}. Moreover, the geometry of the Mn^{III} octahedra will be different from that of the Mn^{IV} octahedra, owing to the Jahn–Teller effect. More details on these effects are to be found in a recent paper by Hervieu *et al.*[6]

Furthermore, it is challenging to expand the investigation of the manganites to other structures related to the perovskite structure but where the overlapping of the Mn–O–Mn occurs in a different way, as in the materials described above. It was indeed found that magnetoresistance occurs in layered perovskite-related structures. In that respect we investigated intergrowths with two perovskite layers and one rocksalt layer with typical structural formulae $Ln_{2-y}A_{1+y}Mn_2O_7$. TEM techniques are excellent for determining the intergrowth structure and to elucidate the local structure of such materials; as we will illustrate, perovskite slabs tend to form between the regular intergrowths, causing doubts about the true magnetoresistance properties of the intergrowth.

Polycrystalline samples of composition $Nd_{2-y}Ca_{1+y}Mn_2O_7$, $Nd_{1.4}Ca_{1.6-x}Sr_xMn_2O_7$ and $Pr_{1.4}Ca_{1.6-x}Ba_xMn_2O_7$ were prepared in the usual way. All materials crystallise in a tetragonal

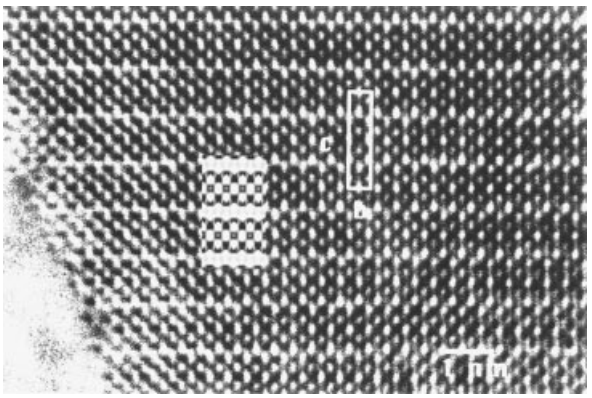

Fig. 13 HREM image along $[100]_p$ of $Pr_{1.4}Ca_{1.45}Ba_{0.15}Mn_2O_7$. The inset shows the calculated image for a defocus of -57 nm and a sample thickness of 5 nm.

average unit cell with $a \approx a_p$; $c \approx 1.93$ nm. Electron diffraction, however, clearly indicates an orthorhombic distortion with lattice parameters $a \approx b \approx \sqrt{2}a_p$. The perfect structure, as viewed by HREM along the $[100]_p$ direction, is shown in Fig. 13; without too much image calculation (shown as inset), the stacking sequence can be deduced immediately. The structure is built up as a sequence of 10 layers, grouped as two blocks of 5 layers shifted over (1/2,1/2,0), *i.e.* the structure is inner centred. The stacking within one block is $AO–MnO_2–AO–AO–MnO_2$, with A = Pr, Ca, Sr (Ba). Alternatively, the structure can be described as a sequence of perovskite blocks, $AMnO_3$, interconnected every two blocks by a rocksalt structured layer.

Electron diffraction detects weak extra reflections pointing to an orthorhombic distortion resulting in an enlarged unit cell; the intensity of these reflections is very variable, even within one crystallite. HREM along [001] or $[110]_p$ clearly reflects this increase of the unit cell. Apart from this change in symmetry, all samples contain a large number of crystal defects, making the local structure sometimes deviate strongly from the average structure. Some of these will certainly influence the physical properties of the materials. We will not discuss here the intergrowth errors, which do not occur very often and which are believed not to be essential for the understanding of the physical properties; neither will we focus on the large number of dislocation loops, which create a high stress inside the material. Details of these can be found in the paper by Laffez *et al.*[7] The main defect, we believe, related to the magnetoresitant properties of these materials is illustrated in Fig. 14. It shows the co-existence of the pseudocubic perovskite structure with general formula $AMnO_3$, as narrow strips of this material within the intergrowth structure (Fig. 14). The interface between both phases is strictly (001) and in view of the lattice match, no strain field or interface dislocation is detected at this interface. Surprisingly, however, the perovskite structure within these nanometer wide strips shows exactly the same local structure as the peroskite single phase discussed above. A doubling of the unit cell along the *b*-axis is present in the HREM images, indicating the same structural deformations as in the bulk; *i.e.* the structure is at least orthorhombically deformed. Also the point-like clusters, discussed above (Fig. 12) and related to the Mn oxidation state, are present within the nanometer sized thin slabs.

$V^V–V^{IV}$ mixed valencies in the ionic conductor $Bi_4V_2O_{11-x}$

$Bi_4V_2O_{11}$ is the parent compound of the so-called BIMEVOX family, exhibiting interesting oxide anion conductivity. All such Bi_2O_3 based oxides are related to the Aurivillius series, where Bi_2O_2 sheets alternate with a perovskite-like layer containing oxygen vacancies which are responsible for the electrical

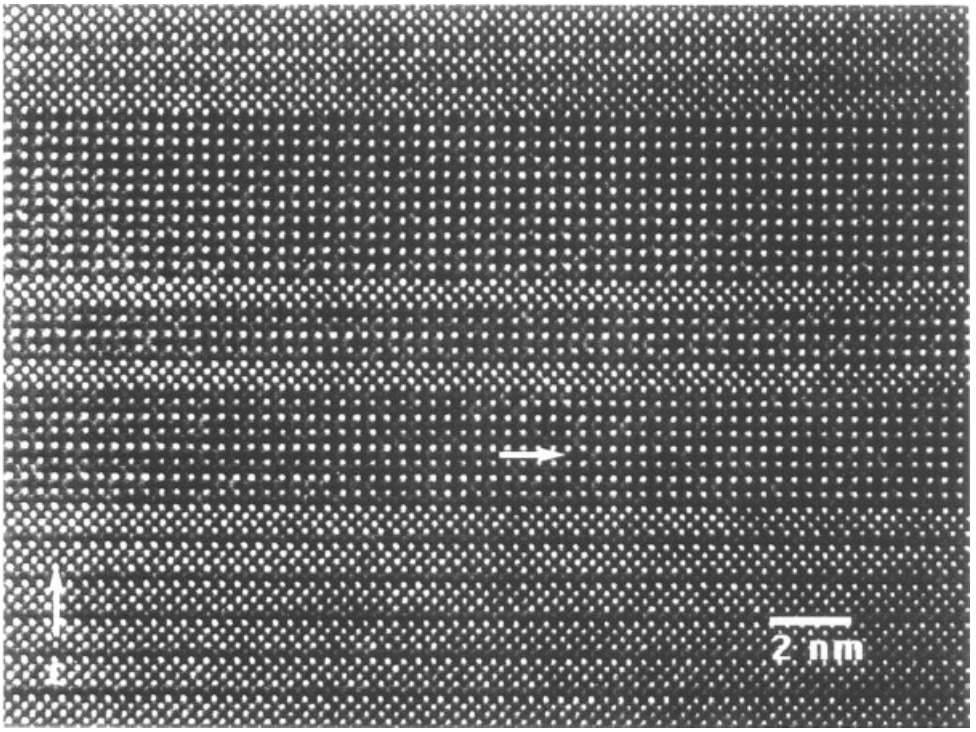

Fig. 14 HREM image along $[100]_p$ of $Pr_{1.4}Ca_{1.45}Ba_{0.15}Mn_2O_7$ showing strips of the perovskite-based phase a few nanometers wide, within an intergrowth structure

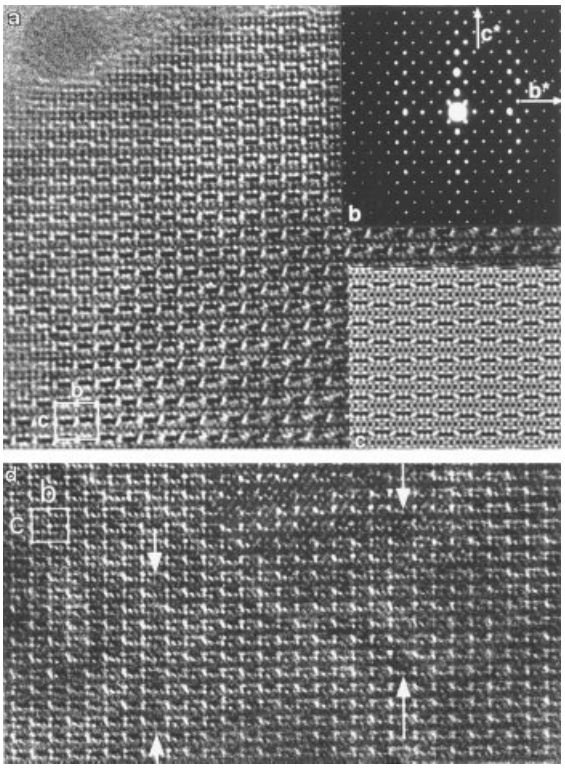

Fig. 15 (*a*) HREM image of $Bi_4V_2O_{10.66}$ along [100]; groups of three vanadium ions are highlighted in the image as black dots between two intense white dots; (*b*) corresponding electron diffraction pattern. (*c*) Computer simulated HREM image for a defocus of 45 nm and a crystal thickness of 5 nm. (*d*) Image of a defective $Bi_4V_2O_{10.66}$; locally blocks of four vanadiums are observed; they are indicated by arrows.

properties of these materials. Although the basic Aurivillius structure is known, the actual structure is more complex, due to the presence of twinning, the formation of incommensurate modulations and problems of stoichiometry. For an overview of the chemical, physical and structural properties, we refer the reader to ref. 8 and references therein.

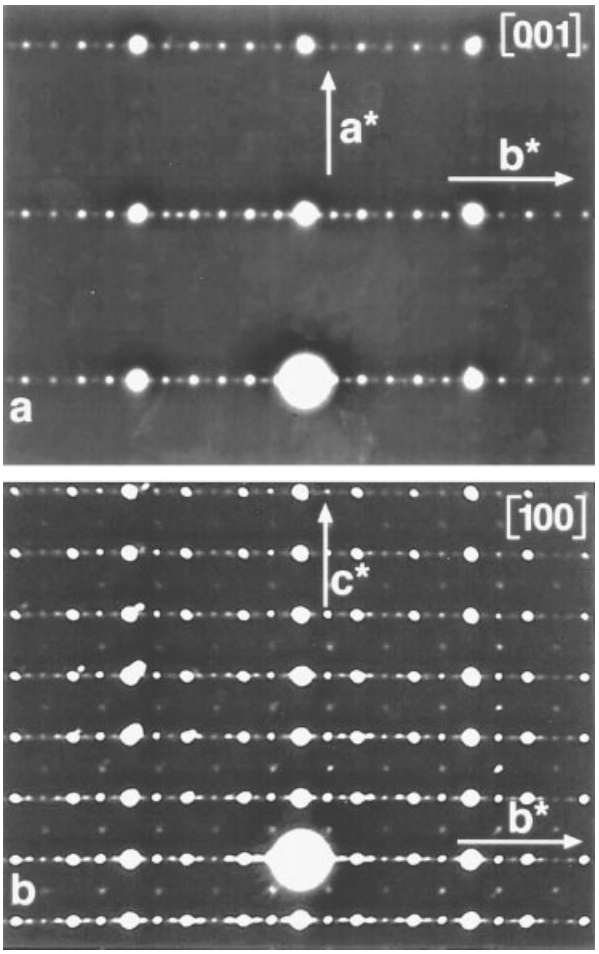

Fig. 16 Electron diffraction patterns of $Bi_4V_2O_{11}$ along [001] and along [100], clearly showing the commensurate modulation along the *b*-axis

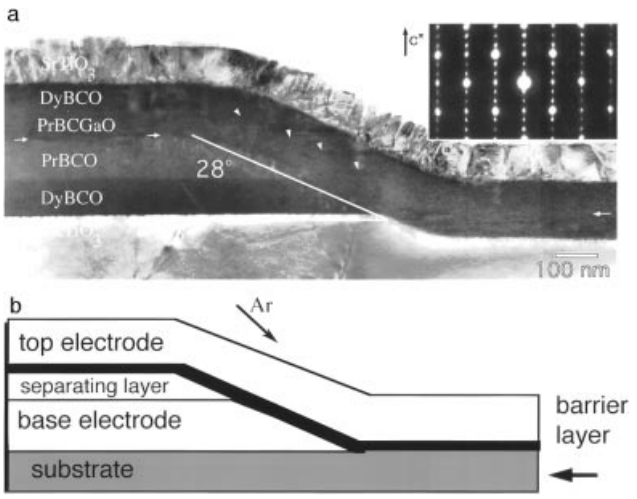

Fig. 17 (*a*) HREM overview of a ramp-type JJ with a PrBCGaO barrier of 10 nm, showing that the interfaces at the ramp are well defined and free of secondary or amorphous phases. (*b*) Schematic representation of the investigated ramp-type junctions.

$Bi_4V_2O_{11}$ is the upper limit of the solid solution $2Bi_2O_3$–xV_2O_5 within the Bi_2O_3–V_2O_5 binary phase diagram; however, pure $Bi_4V_2O_{11}$ is practically never obtained since small traces of $BiVO_4$ are systematically observed. Its 'average' structure is orthorhombic ($a \approx 0.55$; $b \approx 0.56$, $c \approx 1.53$ nm) but three different polymorphs are known as a function of temperature. The main reason for this complexity is likely to be related to the ability of vanadium to undergo a V^V to V^{IV} reduction when the experimental environment is altered by thermal treatment or oxygen partial pressure. This can lead to the formation of mixed valence phases, and ultimately to the formation of $Bi_6V_3O_{16}$ ($Bi_4V_2O_{10.66}$) with $V^{IV}/V^V = 1/2$. Electron microscopy offers the possibility of following the structural changes during *in situ* heating. At any moment of the transformation, the heating can be stopped and the corresponding electron diffraction and corresponding HREM image can be recorded.

The complex [100] diffraction pattern of the reduced material $Bi_4V_2O_{10.66}$ is illustrated in Fig. 15(*b*). together with the corresponding HREM image [Fig. 15(*a*)]; a calculated image based on the available X-ray data for a thickness of 5 nm and a defocus close to the Scherzer defocus is shown as Fig. 15(*c*). The vanadium configuration is highlighted as groups of black dots between two intense white dots. This block of three vanadium atoms along the *b*-direction corresponds to one V^{IV} and two V^V in the structure [see Fig. 15(*a*)]. The waviness of these layers is clearly revealed in the HREM image. This periodicity of one V^{IV} and two V^V is sometimes violated, as in Fig. 15(*d*), where blocks of four vanadium atoms are observed, indicating domains where the reduction of the compound is lower than the ultimate $V^{IV}/V^V = 1/2$. These blocks of four vanadiums [indicated by arrows in Fig. 15(*d*)] likely result from a regular arrangement of one V^{IV} for three remaining V^V. This defect actually introduces an antiphase boundary with $R = 1/3[010]$ in the structure.

The structure of the basic $Bi_4V_2O_{11}$ (the α polymorph) is not entirely clarified; the unit cell has been determined and the heavy V ions located, but the exact oxygen configuration was still unresolved until recently. The structure becomes slightly monoclinic and an extra modulation (6-fold) occurs along the *b*-axis; this is evident from the [001] and the [100] diffraction patterns in Fig. 16. HREM of this phase, however, is barely possible; under the intense electron beam for high resolution observation, a gradual transformation occurs due to the V^V to V^{IV} reduction.

We included this example deliberately to illustrate the problems which may arise with HREM, related to the use of an intense electron beam. Upon heating, the reduction from V^V to V^{IV} is enhanced under the electron beam and the α-phase is no longer stable. In other samples, *e.g.* SiO_2–quartz, ionisation damage is formed very rapidly when studying the material at room temperature; when heating, however, the ionisation damage anneals out faster than the production of new defects and the material is perfectly stable. In this way we have studied without too many problems the phase transition at 573 °C between the α-phase and the β-phase of quartz. When working with an intense electron beam, particularly for a field emission source, one has to realise that this may alter the initial material (even burn a hole in the sample).

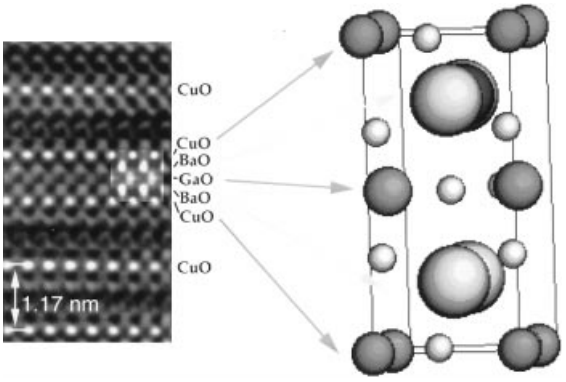

Fig. 18 (*a*) [10] HREM image of the intergrowth of one unit cell of a four layer unit within the 123 structure observed in a PrBCGaO barrier layer ($x = 0.7$). The inset shows a simulated image for $d = 2.4$ nm; $\delta = -25$ nm based on the proposed model (right hand figure).

HREM of inorganic materials with reduced dimensionality

With the progressive miniaturisation of the present technology, systems of reduced dimensionality (thin films, nano-wires or quantum dots) gain more and more interest. The connection (epitaxially or not) between different layers or between layers, wires, dots and the substrate are crucial in determining their properties. High resolution electron microscopy is one of the few techniques which provides real space information down to the atomic level for such interfaces. Moreover HREM contributes to the monitoring of the production of these man-made materials. We will discuss here briefly the problem of growing superconducting Josephson junctions (JJ) on a $SrTiO_3$ substrate. Although this is a specific problem, we hope it will illustrate some of the particular difficulties with nanometer thick films on a substrate.

$YBa_2Cu_3O_7$ Josephson junctions can be fabricated by sandwiching a thin barrier of non-superconducting material between two superconducting electrodes. To be able to interpret correctly the measured properties, one has to perform cross-section HREM in order to obtain local structural information from the junction area itself. However, the cross-section sample preparation of JJ for HREM investigations is not easy, particularly when different layers are deposited. Details on this specific preparation method by ion beam bombardment can be found in refs. 9 and 10.

The preparation of the ramp-type JJ is summarised as follows. The base electrode (DyBCO) and the separating insulating layer (PrBCO) are deposited *in situ*. The ramps are structured by an Ar ion beam source using a photoresist mask. After stripping the photoresist, the ramp surface is cleaned by ion-milling and is re-oxidised *in situ*. Subsequently, the barrier layer (PrBCGaO) and the top electrode (DyBCO) are deposited. The Ga content of barrier layer is nominal. A schematic drawing of the complete ramp-type JJ is shown in Fig. 17, together with the TEM image observed experimentally.

In the PrBCO layer Cu can be substituted by Ga for

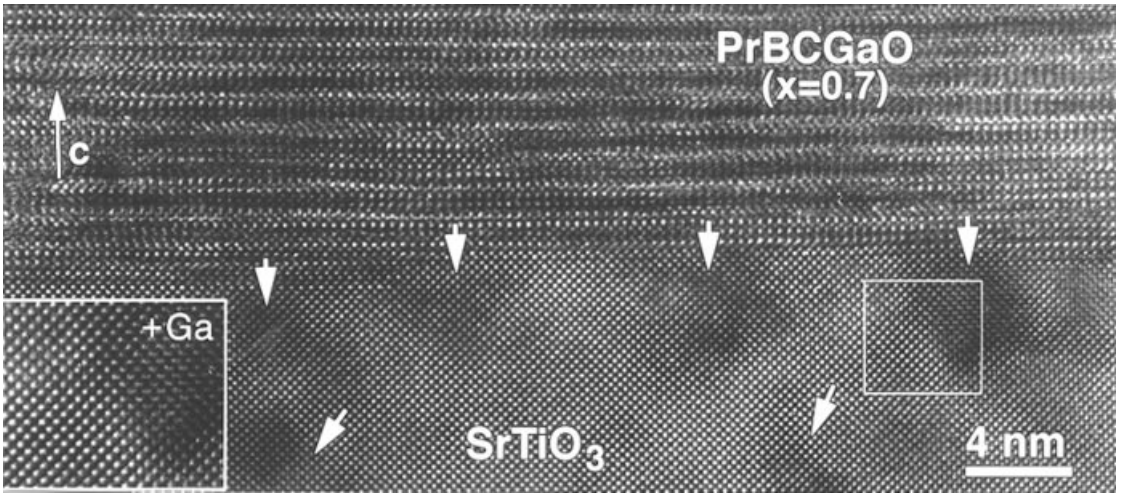

Fig. 19 [001] HREM micrograph of the interface between (a) $PrBa_2Cu_{2.3}Ga_{0.7}O_{7-\delta}$ and ion-etched $SrTiO_3$. Dark contrast Ga-rich areas in the substrate are indicated by arrows.

substitution levels $0.01 < x < 0.9$. XRD shows that bulk $PrBa_2Cu_{3-x}Ga_xO_{7-\delta}$ samples have a structure identical to tetragonal $ReBa_2Cu_3O_{7-\delta}$. No Ga-containing impurity phase is present in PrBCGaO with $x = 0.7$ indicating the full substitution of Cu by Ga. The unit cell parameters are $a = 0.39288(6)$ nm and $c = 1.1756(5)$ nm. For the substitution level $x = 1$ two impurity phases were found, namely CuO and α-$BaGa_2O_4$. The fact that a Ga-containing phase is present as an impurity phase indicates that $x = 1$ is above the maximum substitution level for Ga in $PrBa_2Cu_{3-x}Ga_xO_{7-\delta}$. Bulk $PrBa_2Cu_{3-x}Ga_xO_{7-\delta}$ with $x \geqslant 0.7$ has been carefully investigated by EM and SAED. There is no evidence for any modulation or structural change due to the Ga substitution in the Cu(1) chain.

Electrical properties of ramp-type JJ with PrBCGaO barriers ($x = 0.1$ and 0.4) have been measured. The effect of a PrBCO barrier layer with Ga substitution on the junction parameters is an increase in the resistivity of up to an order of magnitude for the same barrier thickness as compared to junctions with unsubstituted PrBCO as the barrier. However, this trend is not continued for the higher substitution levels $x = 0.7$ and 1. On the contrary, no increase in resistivity for $x = 0.7$ was observed as compared to $x = 0$. The origin of this remarkable fact could only be traced by HREM.

A cross-section TEM investigation provides information about the local structural of the barrier layer as incorporated in the JJ (Fig. 17). No peculiarities were found at the interfaces or inside the superconducting layers responsible for the abnormal behaviour of the JJ with substitution levels $x = 0.7$ or 1 for the barrier layer. The junctions discussed here have a ramp angle of 21°–28° and a typical barrier layer thickness of 10–30 nm. All layers grow epitaxially with the *c*-axis orientation perpendicular to the substrate. All interfaces are sharp and flat. The interfaces between barrier and superconducting layers at the ramp-edge are well defined and free of secondary phases or amorphous layers. This allows us to correlate the observed microstructure of the $PrBa_2Cu_{3-x}Ga_xO_{7-\delta}$ barrier layer and the electrical properties of the ramp-type JJ with this barrier material.

HREM images show that the barrier layer contains isolated unit cells with a *c*-parameter different from c_{123}; a single strip is shown in Fig. 18. These unit cells, with a spacing along the *c*-direction of approximately $c_i = 0.8$ nm, differ from the normal YBCO-123 structure and are not known as common defects in bulk YBCO-123. The intergrowth only occurs in the $PrBa_2Cu_{2.3}Ga_{0.7}O_{7-\delta}$ barrier layer, not in the DyBCO bottom or top layer nor in the PrBCO separating layer. If the Ga content is increased the density of this type of intergrowth is also increased. The presence of Ga apparently favours the presence of the intergrowth. HREM combined with local microanalysis allows us to propose a model for the Ga-containing intergrowth layer. The unit cell for this new structure is reproduced in the right hand part of Fig. 18. There is a clear inequivalence in contrast between the CuO planes and the plane in the middle of the intergrowth unit cell. The contrast above and below the CuO planes is similar. The contrast strongly resembles a double perovskite with an inequivalent lattice plane in the middle of the cell. This was interpreted as showing the occurrence of a full Ga plane. A model with layer stacking PrBCO–CuO–(Pr,Ba)O–GaO–(Pr,Ba)O–CuO–PrBCO, based on one slab of $(PrBa)CuGaO_z$ sandwiched between PrBCO unit cells, was created and image simulations were carried out. Ga and its surrounding oxygens were shifted from the ideal perovskite positions due to the tetrahedral co-ordination of Ga. The computer simulated images based on this model yield good agreement with the observed HREM image (see the inset in the image of Fig. 18).

Within the $SrTiO_3$ substrate, pronounced black patches are observed in the uppermost 10 nm of the interface region with the barrier layer (see Fig. 19). This specific contrast exists in all parts of the $SrTiO_3$ substrate, even on the inclined ramp-edge in $SrTiO_3$, which have been exposed to Ar etching to create the ramp-edges. Such contrast variations are not observed normally for ReBCO films on $SrTiO_3$ and we can eliminate ion-beam thinning sample preparation as a possible origin. Possible other causes could be oxygen depletion, or interdiffusion either of the photoresist material or of gallium from the barrier layer. The contrast of the black patches is only observed for the combination of a Ga-containing layer on an ion-etched $SrTiO_3$ substrate. Therefore, we believe that Ga diffusion in the surface region of the ion-etched $SrTiO_3$ substrate is the reason for the local structural distortions. This can be understood if we assume that lattice imperfections, such as oxygen vacancies or point defects, which are created in the $SrTiO_3$ substrate by the ion-etching, facilitate the diffusion of gallium in the interface region of the substrate.

We conclude that two distinct mechanisms of Ga segregation in thin barrier layers are operative; the formation of a Ga-containing intergrowth in the barrier layer itself and diffusion of Ga in the ion-etched substrate. The microstructure of $PrBa_2Cu_{3-x}Ga_xO_{7-\delta}$ ($x = 0.7$ or 1) thin barrier layers is clearly different from that in the bulk material. $PrBa_2Cu_{3-x}Ga_xO_{7-\delta}$ with $0.1 \leqslant x \leqslant 0.4$ can be used as barrier layer in ramp-type

Josephson junctions to enhance reproducibly the normal state resistivity. However, higher Ga substitutions are not effective.

This example of the Josephson junction on a $SrTiO_3$ substrate illustrates the possibilities of HREM in the study of the structural aspects related to the deposition of a thin layer or sequences of thin layers on a given substrate. Other interesting phenomena which are beneficially studied by TEM include the change of growth mechanism as a function of temperature, the deposition and growth of diamond thin films, the study of semiconductor devices, the growth of (carbon) nanotubes or the characterisation of nanometer or sub-nanometer sized particles.

Future of HREM in materials science

Since the discovery of electron microscopy in 1931, the instrumental resolution has decreased steadily, to reach the atomic level in the seventies and the 1 Å level in the nineties. However, to prove this 1 Å resolution limit, a strongly scattering sample with a minimal thickness (preferentially in the 1 nm range) is required. It is my personal impression that the future of electron microscopy for materials science is not so much in improving the ultimate resolution below the mythical 1 Å but should rather concentrate on: (i) a correct and 'user friendly' interpretation of the high resolution images down to the instrumental resolution. The feasibility of this has been proven[3] but 'everyday use' has still some way to go; (ii) a quantitative interpretation for the combination of electron diffraction and HREM. With CCD cameras becoming more and more standard, the evolution of this will be more or less straightforward; (iii) the use of the electron–sample interaction to its full capacity, *i.e.* we shall no longer limit ourselves to the transmitted and the elastically scattered electron beams, but also use the information available in the emerging X-rays, inelastically scattered electrons, secondary electrons, backscattered electrons, light, *etc*. Although a lot of progress has been made on this matter, I believe it will strongly contribute to the future success of transmission electron microscopy.

I would like to thank my co-workers at the EMAT research centre of the University of Antwerp (K. Verbist, P. Laffez, M. Huvé, O. I. Lebedev, D. Van Dyck, J. Van Landuyt and S. Amelinckx), as well as collaborators from outside the University (D. Blank, R. V. Shpanchenko, E. V. Antipov, M. Hervieu) for the use of results from common publications. Financial support is provided by IUAP 4/10.

References

1 *Handbook of Microscopy*, ed. S. Amelinckx, D. Van Dyck, J. Van Landuyt and G. Van Tendeloo, VCH, Weinheim, 1997.
2 *Electron Diffraction Techniques*, ed. J. M. Cowley, Oxford University Press, 1993.
3 H. W. Zandbergen, S. J. Andersen and J. Janssen, *Science*, 1997, **277**, 1221.
4 D. Van Dyck, in *Electron Microscopy*, ed. S. Amelinckx, D. Van Dyck, J. Van Landuyt and G. Van Tendeloo, VCH, Weinheim, 1997.
5 R. V. Shpanchenko, M. G. Rozova, A. M. Abakumov, E. I. Ardashnikova, M. L. Kovba, S. N. Putilin, E. V. Antipov, O. I. Lebedev and G. Van Tendeloo, *Physica C*, 1997, **280**, 272.
6 M. Hervieu, G. Van Tendeloo, V. Caignaert, A. Maignan and B. Raveau, *Phys. Rev. B*, 1996, **53**, 14274.
7 P. Laffez, G. Van Tendeloo, R. Seshaddri, M. Hervieu, C. Martin, A. Maignan and B. Raveau, *J. Appl. Phys.*, 1996, **80**, 5850.
8 M. Huve, R-N. Vannier, G. Nowogrocki, G. Mairesse and G. Van Tendeloo, *J. Mater. Chem.*, 1996, **6**, 1339.
9 K. Verbist, O. I. Lebedev, G. Van Tendeloo, M. A. J. Verhoeven, A. J. H. M. Rijnders and D. H. A. Blank, *Supercond. Sci. Technol.*, 1996, **9**, 978.
10 K. Verbist, O. I. Lebedev, G. Van Tendeloo, M. A. J. Verhoeven, A. J. H. M. Rijnders, D. H. A. Blank and H. Rogalla, *Appl. Phys. Lett.*, 1997, **70**, 1167.

Paper 7/08240A; *Received* 17*th November*, 1997